

Measuring Muon-Induced Neutrons with Large Liquid Scintillation Detector at Soudan Mine

C. Zhang^{1,2} and D.-M. Mei^{1,3,*}

¹ *Department of Physics, The University of South Dakota, Vermillion, South Dakota 57069*

² *College of Sciences, China Three Gorges University, Yichang 443002, China*

³ *College of Physics, Yangtze University, Jingzhou 434023, China*

We report a first direct detection of muon-induced high energy neutrons with a 12-liter neutron detector fabricated with EJ-301 liquid scintillator operating at Soudan Mine for about two years. The detector response to energy from a few MeV up to ~ 20 MeV has been calibrated using radioactive sources and cosmic-ray muons. Subsequently, we have developed an approach to calculate the scintillation efficiency for nuclear recoils up to a few hundred MeV. Data from an exposure of 655 days were analyzed for high energy neutrons using pulse shape discrimination which allowed us to detect muon-induced fast neutrons with energy up to a few hundred MeV for the first time. The muon-induced fast neutron flux for neutron energy greater than 10 MeV is measured to be $(4.73 \pm 1.1(\text{sta.}) \pm 0.4(\text{sys.})) \times 10^{-9} \text{ cm}^{-2} \text{ s}^{-1}$, in a reasonable agreement with the model prediction. The muon flux is found to be $(1.65 \pm 0.02(\text{sta.}) \pm 0.1(\text{sys.})) \times 10^{-7} \text{ cm}^{-2} \text{ s}^{-1}$, consistent with other measurements. As a result, the muon-induced high energy gamma-ray flux is simulated to be $7.08 \times 10^{-7} \text{ cm}^{-2} \text{ s}^{-1}$ for the depth of Soudan.

PACS numbers: 95.30.Cq, 14.20.Dh, 98.70.Vc, 29.40.Mc

I. INTRODUCTION

Measuring muon-induced fast neutrons is important to the understanding of backgrounds for many rare event physics experiments including directly searches for dark matter. Dark matter is believed to account for about a quarter of the mass-energy budget of the known universe [1]. However, the nature of dark matter is still mysterious to us so far. As a candidate of dark matter, Weakly Interacting Massive Particle (WIMP) is a target for direct detection through a set of underground experiments. Some of them, such as DAMA [2], CDMS-Si [3], CoGeNT [4], and CRESST-II [5] have claimed positive results while others including CDMS-Ge, Xenon100, LUX [12–14], and SuperCDMS [15] have ruled out those claims. Many experiments have set an upper limit on the mass cross-section contour of WIMPs interacting with normal matters [6–15]. The next generation ton-scale experiments aim to achieve a sensitivity of $\sim 10^{-48} \text{ cm}^2$ WIMP-Nucleon cross-section for WIMP mass of ~ 100 GeV.

Understanding the background events is the key to the success of any dark matter search experiment. Because they behave in a manner similar to WIMPs, fast neutrons are taken as a vital background for these rare event physics experiments at deep underground. Although the cosmogenic effects are dramatically suppressed by rock overburden [16], the energy spectrum, angular and multiplicity distribution of the fast neutrons induced by muons underground are not well understood [16–23]. Muon-induced neutron production rates in different targets have been recently measured by many experiments [24–

26] through measuring neutron captures. The direct measurements of neutron energy spectrum have not yet been reported. The muon-induced fast neutrons with energy above ~ 10 MeV are difficult to shield and can contribute to the total background budget for a given experiment. The fast neutrons, from (α, n) reaction and fission decay in the surrounding rocks, are lower in energy and thus easier to stop. To characterize those neutrons as a source of background for dark matter experiments in an underground environment by deploying a neutron detector in-situ will definitely help the understanding of the experimental results.

A neutron measurement usually involves identity discrimination using scintillation detectors and energy scaling utilizing the time of flight (TOF) technique. However, the TOF measurement will largely limit the acceptance of neutrons. Because of the low neutron intensity at deep underground sites, a neutron detector with large detection efficiency is needed. In addition to the TOF technique, the recoil energy of ions in liquid scintillators can represent the energy of incident neutrons if the detector response to nuclear recoils is well understood with a Monte Carlo simulation. Therefore, a large liquid scintillation detector holds promise to directly measure fast neutrons in a deep underground environment.

The light response to nuclear recoils caused by neutrons within liquid scintillators are usually measured using the TOF technique or the unfolding method. The latter one requires a response function to unfold the visible energies “seen” by PMTs to the recoil energy caused by incident neutrons. Such a function has been widely studied for neutron energies from a few MeV to several hundred MeV [27–32] with small scintillation detectors (several liters). Several Monte Carlo codes such as CECIL [27], O5S [33] and SCINFUL [34] are developed to calculate the neutron response function in liquid scintil-

*Corresponding Author: Dongming.Mei@usd.edu

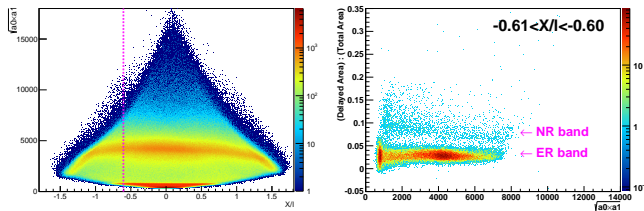


FIG. 1: The left plot is the detector response to scintillation light versus the position for a surface background run with a live time of 19.4 days. The right plot shows the separation of Nuclear Recoils (NR) and Electron Recoils (ER) for a position range $-0.61 < X/l < -0.60$. The position range is also marked as the dashed lines in the left plot.

lators.

Aimed at characterizing fast neutrons at deep underground sites, a large-scale neutron detector has been fabricated at the University of South Dakota (USD). It consists of an aluminum tube, one meter long and 5 inches in diameter, filled with 12 liters EJ-301 liquid scintillator. Two 5-inch Hamamatsu PMTs (R4144) are attached to both ends of the tube through Pyrex windows to collect the scintillation light. Detailed calibration procedures and neutron-gamma separation techniques are discussed in Ref. [35]. In this paper, the detector responses to atmospheric neutrons are studied. We show the measured nuclear recoils with energy up to ~ 50 MeV for the first time using two years data collected at the Soudan Mine.

II. ENERGY CALIBRATION FOR HIGH ENERGIES

A background run with a live time of 19.4 days was conducted in a surface building at the USD campus prior to moving the detector underground. Following the calibration strategy we developed in Ref. [35], the detector responses to scintillation lights are shown in FIG. 1. An example of NR/ER discrimination from a very narrow position range is also shown in the right plot. This liquid scintillation detector is calibrated from 1 MeV to 20 MeV by using ^{22}Na (1.275 MeV), AmBe sources (4.4 MeV), and the minimum ionization peak from cosmic muons (20.4 MeV). Applying the position independent variable $\sqrt{a0} \times a1$, where $a0$ stands for the total charge converted from PMT0 and $a1$ is the total charge converted from PMT1, a second order polynomial function is assumed to fit the calibration curve for energy below 20 MeV. For energies above 20 MeV, the first order approximation is a simple extension from the low energy calibration curve. Considering the background signals with the energy above 10 MeV are dominated by the well-understood surface muons, the calibration curve above 20 MeV is then justified by the detector response to the surface muons. A GEANT4 [36] based simulation is conducted with a modified Gaisser's formula [37] (sea level)

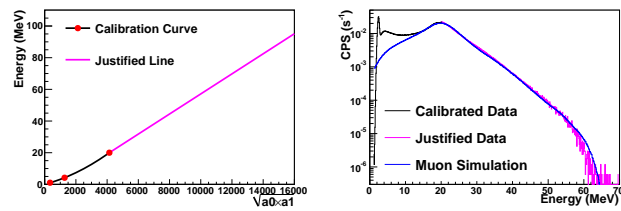


FIG. 2: The left plot is the calibration curve of the light output versus the energy deposition in the detector. The lower energy curve (< 20 MeV) is fitted by the three calibration sources. The higher energy curve (> 20 MeV) is justified by the simulation. The right plot is the comparison of detector response to muons between the simulation and data.

to sample the shape of the energy spectrum and angular distribution of input muons. The simulated detector response to muons is compared with data by assuming a linear relation between the light output $\sqrt{a0} \times a1$ and the energy deposition (> 20 MeV) in the detector. The slope of the calibration line (> 20 MeV) is then determined by fitting the detector response to the simulated muons with the corresponding data.

The plots in FIG. 2 demonstrate how the high energy calibration line (left) is determined by fitting data with the simulation (right). For the lower energy range (< 10 MeV), the data are overwhelmed by the internal contamination and environmental gamma rays, which explains why the data and the muon simulation do not match at such range. It is worth mentioning that the absolute normalization of the detected muon intensity is 16.6% higher than the flux from sea level. This is reasonable because the surface muon data was taken at the campus of the University of South Dakota with an elevation of 1221 feet [38] above the sea level.

Applying the entire energy calibration curve and the algorithm developed in Ref. [35], the plots in FIG. 3 present the calibrated gamma rays and neutrons with a surface background run for 19.4 days. Utilizing the calibrated energy scale, we can assume that the linear relation between the energy deposition and the light output is the same for electron recoils and nuclear recoils. NR/ER separation at different positions is compared which concludes that a better separation can be achieved when the positions are closer to the PMTs.

III. LIGHT OUTPUT RESPONSE TO FAST NEUTRONS

The results from the surface background run in FIG. 3 show the separation of nuclear recoils from electron recoils. After selecting only those events from the NR band, the visible energy from nuclear recoils in the detector is shown in FIG. 4 (solid dots). The cut-off at ~ 2 MeV is caused by energy threshold set on the trigger while the waterfall at 60-70 MeV is caused by the saturation

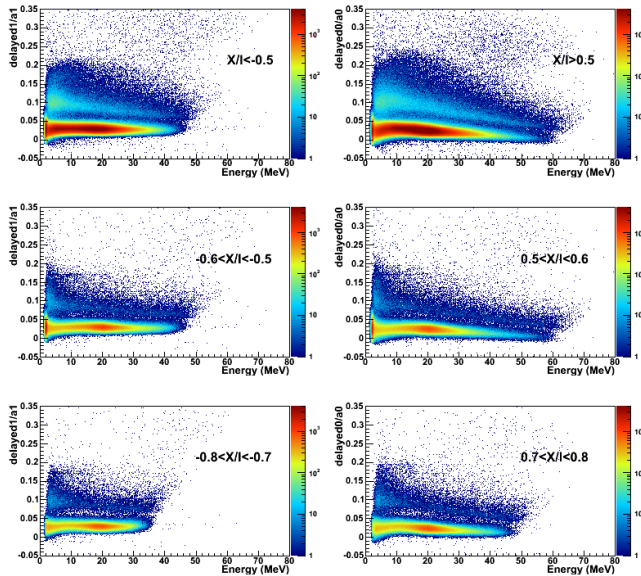


FIG. 3: The detector response to surface background at different position range. The left three plots collect the events with the positions at $X/l < -0.5$, $-0.6 < X/l < -0.5$ and $-0.8 < X/l < -0.7$ through the PMT1 while the right three plots collect the events with the positions at $X/l > 0.5$, $0.5 < X/l < 0.6$ and $0.7 < X/l < 0.8$ through the PMT0. It's a surface background run with a live time of 19.4 days.

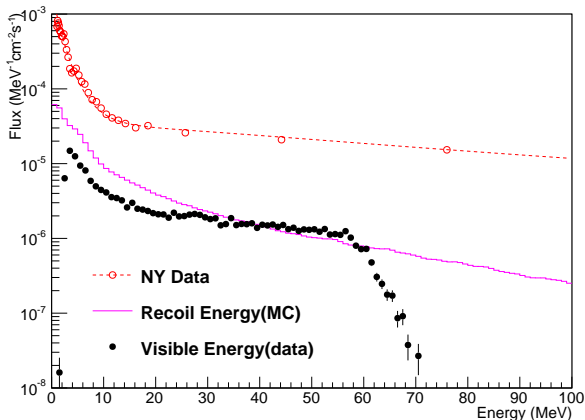


FIG. 4: The detected visible energy (solid dots) compared with the simulated recoil energy (solid line). The input neutron energy spectrum from the surface measurement in New York city is also listed (dashed line with open dots).

of the Analog-to-Digital Converter (ADC) channels. A simulation is performed by adopting the neutron energy spectrum from Ref. [53] as an input. Although it is a neutron measurement in New York city, it can serve as a reasonable approximation by taking just the shape of the neutron energy spectrum with the intensity to be determined later by comparing the simulated detector response to the experimental data.

The nuclear recoils from neutrons in the detector are simulated and the result is shown in FIG. 4 (solid line). No cuts are applied to the simulated curve yet since we need to understand the light output response from nuclear recoils. The measured visible energy to nuclear recoils is also shown in FIG. 4 (black dots). A quenching factor matrix exists between the recoil energy and the visible energy “seen” by the PMTs. The light output in the liquid scintillator can be described by Birks relation [40]:

$$\frac{dL}{dx} = \frac{S \frac{dE}{dx}}{1 + kB \frac{dE}{dx}}, \quad (1)$$

where $\frac{dL}{dx}$ represents the light output per unit path length, S stands for the scintillation efficiency and $\frac{dE}{dx}$ is the specific stopping power. kB is called Birks constant for the specified medium. The quenching factor for nuclear recoils is defined as the ratio of light yield of ions to that of electrons of the same energy [41]. This definition allows us to calculate the quenching factor by rewriting Eq. (1) as:

$$Q_i = \frac{L_i(E)}{L_e(E)} = \frac{\int_0^E \frac{dE}{1 + kB(\frac{dE}{dx})_i}}{\int_0^E \frac{dE}{1 + kB(\frac{dE}{dx})_e}}. \quad (2)$$

The Birks constant kB is believed to be the same for all ion recoils in the same medium. For the liquid scintillator EJ-301, it has been measured to be $\sim 161 \mu\text{m}/\text{MeV}$ [42]. The interactions of a fast neutron in the liquid scintillator are dominated by multiple scattering processes and therefore generate multiple ion recoils (see FIG. 5). This means that even if the total recoil energy is the same, it could be composed of single or multiple ion recoils which have different quenching factors in the scintillator. Theoretically, a combined quenching factor could be calculated if we track all scattering processes in simulations. Other than the Birks constant, the other remaining variable is the stopping power for each ion in the scintillator. FIG. 6 summarizes the dE/dx functions obtained from the simulations. The stopping power converted from the NIST web database ESTAR, PSTAR and ASTAR for electrons, protons and alphas in scintillators are also listed, respectively. Within the web database, the material most similar to EJ-301 is the plastic scintillator. Therefore we take the mass stopping power of the plastic scintillator and convert it to be the stopping power for the liquid scintillator simply by applying the density of EJ-301 scintillator. The comparison in FIG. 6 shows that the stopping power function for alpha(ASTAR) and proton(PSTAR) have a reasonable agreement with the calculations from GEANT4 simulation. However the stopping power of electrons shows differences, especially at high energies, by a factor of 2. This discrepancy is likely caused by the different models used to calculate the stopping power. The stopping power we used to calculate the quenching factors are all from GEANT4 simulations.

By applying Eq.(2) step by step for each nuclear recoil event in the simulation, a combined quenching fac-

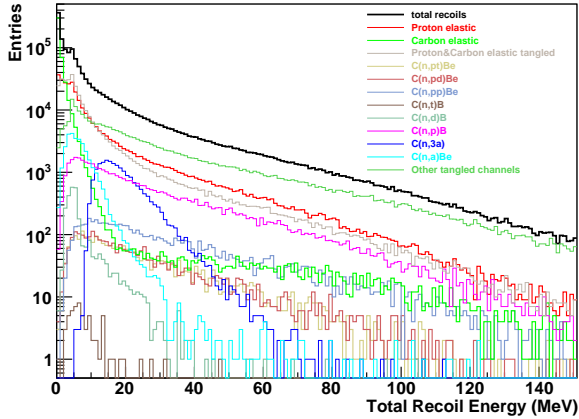


FIG. 5: The number of interaction types in the nuclear recoil events. The total recoil energy is defined as a sum of all energy deposition of the event which contains at least one ion scattering in the scintillator. This is a simulation result by adopting the incident neutron flux from Ref. [53]. The energy threshold of the input neutrons is set to be 4 MeV.

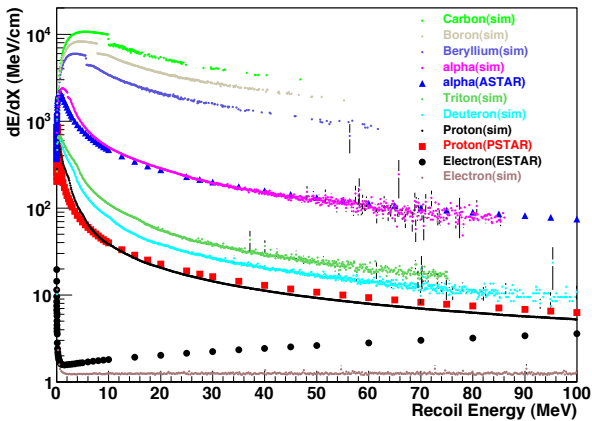


FIG. 6: Stopping power obtained from simulations for carbon, boron, beryllium, alpha, triton, deuteron, proton and electron in the EJ-301 scintillator. As a comparison, the stopping power from ESTAR [43], PSTAR [44] and ASTAR [45] for electron, proton and alpha in plastic scintillators are also shown, respectively.

tor function is generated as shown in FIG. 7. For the recoils with energy in the range of MeV, carbon scattering plays an important role in terms of quenching effect which drives the quenching factor much lower when compared to that of the proton only. When the recoil energies approach ~ 13 MeV, $C(n,3\alpha)$ processes start to build up. The combined quenching factor of multiple α s has an even lower quenching factor when compared to single α with the same total recoil energy in the scintillator. This explains why there is a “knee” at such an energy range. For high energy recoils, the most of the energy

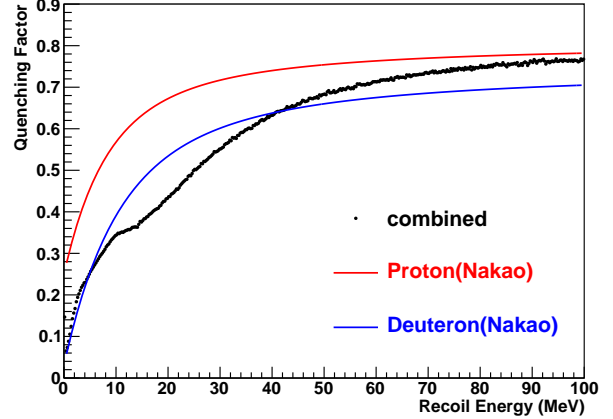


FIG. 7: The combined quenching factor for EJ-301 scintillator calculated from simulations (black dots). The parametrized quenching function for proton (red line) and deuteron (blue line) in EJ-301 scintillator [32] are also plotted.

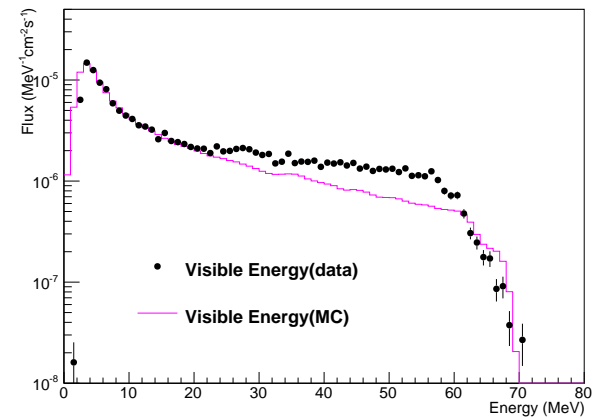


FIG. 8: Comparison between the measured data (solid dots) and the simulation (solid line) for the visible energy of nuclear recoils.

is taken by proton scatterings which make the combined quenching effect approaching to that of proton recoil in this range.

Applying the calculated quenching factor to each ion recoil in the simulation, the simulated visible energy is obtained and compared with the data (see FIG. 8). The simulated results show a good agreement with data for the energies below 20 MeV. For the energies above 20 MeV, the current simulation yields less nuclear recoil events by a factor of ~ 2 than that of data. There are two reasons that may cause such a discrepancy. One is the limited understanding of the detector response to high energy neutrons, such as energy and position reconstructions. The other is the input source in which we only implemented neutrons in the simulation that ignored nu-

clear recoils induced by other possible sources such as protons, alphas, and high-energy gammas.

IV. MUON AND NEUTRON MEASUREMENTS AT SOUDAN MINE

The Soudan underground laboratory is located at a 690 m deep (2100 m.w.e) underground facility in the Soudan Mine, Minnesota. Several underground experiments such as MINOS [46], CDMS [47], and CoGeNT [48] are running there. With such a large rock overburden, the background from cosmic-ray muons is dramatically suppressed. The muon flux at Soudan Mine was measured to be $1.77 \times 10^{-7} \text{ cm}^{-2} \text{ s}^{-1}$ from the MINOS far detector [49]. The neutron flux in the laboratory is dominated by the radioactivity from the surrounding rocks through (α, n) reactions and fission decays which have the most of energies below 10 MeV. For those neutrons with higher energies, the production comes primarily from cosmic-ray muons through spallation processes.

A. Simulation of muons and the muon-induced secondaries

The high-energy particles produced underground are induced by cosmic-ray muons which penetrate from the Earth's surface down to the mine. The intensity of these muons varies from one location to another depending on the altitude and profile of the mountains on the surface as well as the rock densities along the path of muons. In order to quantify those cosmogenic events, a full GEANT4-based simulation has been conducted by adopting the surface mountain profile from the CGIAR satellite data [50] with the extension of $20 \text{ km} \times 20 \text{ km}$ as shown in FIG. 9. Note that a PeV muon has a travel distance $6 \sim 7 \text{ km}$ in rocks on average. A 10 km radius would be sufficient to serve our simulation purpose. According to the information provided by MINOS experiment, its far detector situates at (longitude: $92^{\circ}14'28.51443'' \text{ W}$, latitude: $47^{\circ}49'13.25409'' \text{ N}$) [51]. A 20 m^3 cavern is assumed with the center located at $(0, 0, -217 \text{ m})$ in the map. A typical rock composition of Ely Greenstone is selected with an average rock density of 2.85 g/cm^3 [52] in the simulation. Muons sampled from the modified Gaisser's formula [37] are then tracked from the surface of the mountains down to the cavern. Finally, muons and the associated secondaries are collected at the edge of the cavern with their energy and angular distribution displayed in FIG. 11.

The top-left plot in FIG. 11 compares the energy spectrum of the simulated muons in the cavern with the associated secondary neutrons and gamma-rays. The energy scale of the muons is in GeV while the neutrons and gamma-rays are in MeV. The comparison of their multiplicities in the top-right plot reveals the muon shower information:

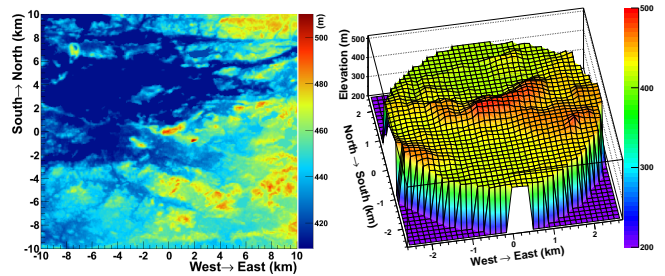


FIG. 9: Shown is a digitized elevation map around the Soudan Mine area from the satellite data [50]. The total extension of $20 \text{ km} \times 20 \text{ km}$ is used in the simulation (left plot). The right plot is a zoomed-in view of the central area.

TABLE I: Parameters for the analytic model in Eq. 3

j	β_j	γ_j	c_j
1	0.3500	2.1451	4.6283e-13
2	0.4106	-0.6670	1.0097e-09

- The relative ratios for the production of neutrons and high-energy gamma rays are counted to be $N_\mu : N_n : N_\gamma = 1 : 0.0115 : 0.715$, which means that there are 1.15% of primary muons generated neutrons and 71.5% of primary muons generated gamma rays at the depth of Soudan.
- The average multiplicity per muon-induced event is $M_\mu : M_n : M_\gamma = 1.0 : 2.6 : 9.9$, which means that the average multiplicity for neutrons is about 2.6 and for gamma rays is about 9.9.
- The angular distribution in the bottom plots indicate the lateral correlation between the primary muon and its secondaries. Comparing to the neutrons, the gamma rays are more peak-forwarded with respect to primary muons. The angular distribution of neutrons show a little correlation with respect to primary muons angular distribution.

The reconstructed neutron energy spectrum from the Monte Carlo simulation can be expressed using an analytic model suggested in Ref. [53]:

$$\frac{d\Phi(E)}{dE} = \sum_{j=1}^2 c_j \exp[-\beta_j (\ln(E))^2 + \gamma_j \ln(E)], \quad (3)$$

where the values of c_j , β_j , and γ_j are listed in Table I. Note that c_j is a normalization factor which is determined by fitting the neutron energy spectrum using Eq. 3, β_j and γ_j are the parameters suggested in Ref. [53].

By normalizing the live time to that of the input muons at the surface level, the absolute fluxes for the muons, neutrons and gamma rays in the cavern are obtained to be $1.99 \times 10^{-7} / \text{cm}^2 / \text{s}$, $5.72 \times 10^{-9} / \text{cm}^2 / \text{s}$, and $8.57 \times 10^{-7} / \text{cm}^2 / \text{s}$, respectively. Although there are uncertainties

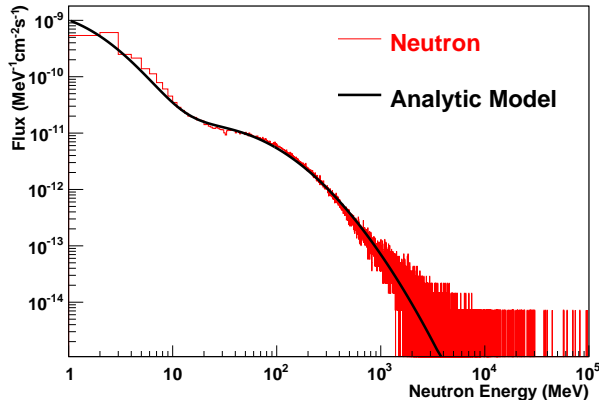


FIG. 10: Reconstructed neutron energy spectrum at the depth of Soudan Mine (the red line). The black line is the fitted analytic function.

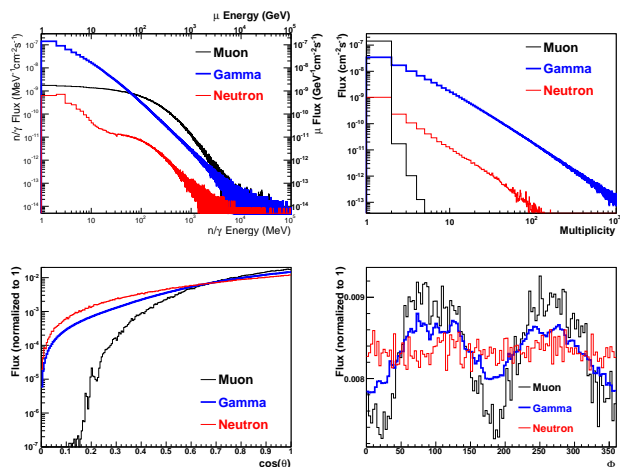


FIG. 11: Energy and angular distribution of the muons and the associated neutrons, gamma rays in the cavern at the depth of Soudan from the Monte Carlo simulation. The energy scale of muons is in GeV while that of neutrons and gamma rays are in MeV. θ is defined as the zenith angle to the vertical direction (downwards). Azimuthal angle Φ is defined as an observation angle to the east direction. $\Phi = 0$ stands for particles come from the east while $\Phi = 90$ represents particles come from the north.

from the input muon intensity and the rock density variations, the simulated fluxes serve as a first order of approximation for the intensity of muons and the induced secondaries in the cavern. The uncertainties can be justified by measurements. However the shape of their energy and angular distributions are in agreement with Ref. [16] and the muon angular distribution agrees with a measurement made by Ref. [54]. FIG. 12 shows the shape of azimuthal angle distribution compared with a measurement [54] made by using an active muon veto shield (room) at the Soudan Mine where the neutron detector

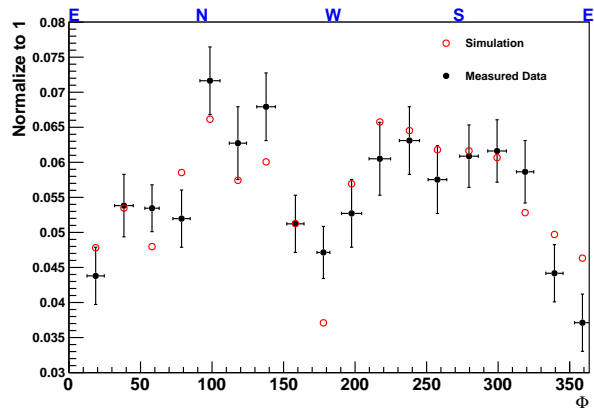


FIG. 12: Comparison of muon azimuthal angle distribution at Soudan Mine. The solid dots are from the experimental data measured using an active muon veto [54]. The empty dots are from the simulation result. The total fluxes are both normalized to 1. The orientation of muons from the East, North, West and South are denoted at the top.

situates inside. The bin size of the simulated azimuthal angle is reorganized according to that of the measurement data. A reasonable match is found which demonstrates the reliability of the simulations.

B. Measurement Results

The detector has been taking data at the Soudan underground laboratory for about two years. The detector response to nuclear recoil (NR) and electron recoil (ER) is measured and shown in FIG. 13. For those nuclear recoils occurring far from the PMTs (the middle of the tube), the difference in their pulses is easier to be washed out due to the scattering and attenuation processes of photons on their way to the PMTs. Therefore their energy threshold of NR/ER separation is relatively higher than the events occurring closer to the PMTs. The left plot shows only the events with their position range $|X/l| > 0.5$ in order to get better NR/ER separation especially for low energies. A 4 MeV energy threshold is set for good NR/ER separation in the left plot while a 6 MeV energy threshold is applied in the right for events from the entire detector. The events from the nuclear recoil band (see FIG. 13) are limited by the statistics. For those events with their visible energy below 4 MeV, the characterized ratio, $(DelayedArea) : (TotalArea)$, suffers severely from the random noise which is superimposed on the signal pulses.

The events from ER band in FIG. 13 (right plot) are picked out and normalized according to their live time. The corresponding energy spectrum is displayed in FIG. 14 (solid dots). Taking the muons and the associated secondaries in the cavern as the input of simulation,

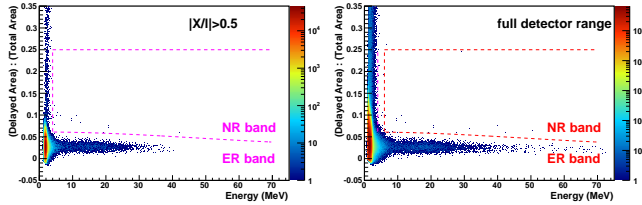


FIG. 13: Shown are the measurements of neutrons and gamma rays at Soudan Mine with a live time of 655.1 days. The position of the events in the left plot are restricted to $|X/l| > 0.5$. The events in the right plot are from the entire detector. The energy threshold for NR/ER separation is set to 4 MeV in the left plot and 6 MeV in the right plot.

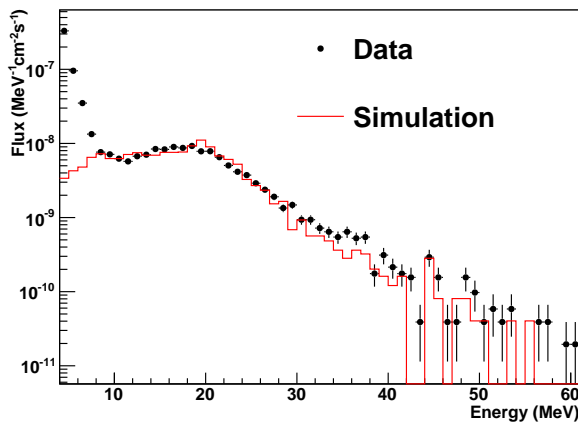


FIG. 14: The electron recoil events (solid dots) obtained from the ER band in FIG. 13. Detector response from the muon simulation (solid line) is normalized to the high energy region (>10 MeV) of the data. The normalization was performed using the simulation divided by a factor of 1.21.

the detector response to muon showers in the cavern is conducted with the result normalized to ER data (> 10 MeV) as shown in FIG. 14 (red line). The simulated ER response to the muon shower is found to be a factor of 1.21 higher comparing to the measurement data. Taking this factor into account we justify the absolute muon flux at the cavern from 1.99×10^{-7} /cm²/s to 1.65×10^{-7} /cm²/s while we still keep the shape of muon energy and angular distribution in FIG. 11.

Muon electromagnetic showers produce a large amount of secondary particles which can contribute to nuclear recoils in liquid scintillators. General speaking, neutron elastic/inelastic processes are considered to be the dominated NR interaction channels comparing to muon-nucleus and photo-nuclear interactions. The simulation finds that muon showers contain a factor of 100 more gamma rays than neutrons. Considering this intensity factor and the interaction cross section in liquid scintillators, these secondary high-energy gamma rays have non-negligible contributions to nuclear recoils in the de-

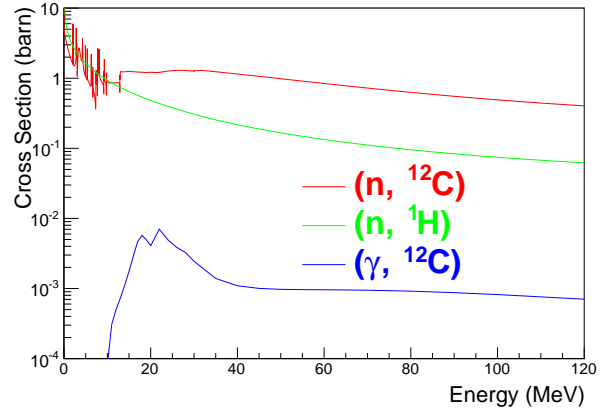


FIG. 15: The comparison of the interaction cross sections [57] for neutron and gamma ray in liquid scintillators.

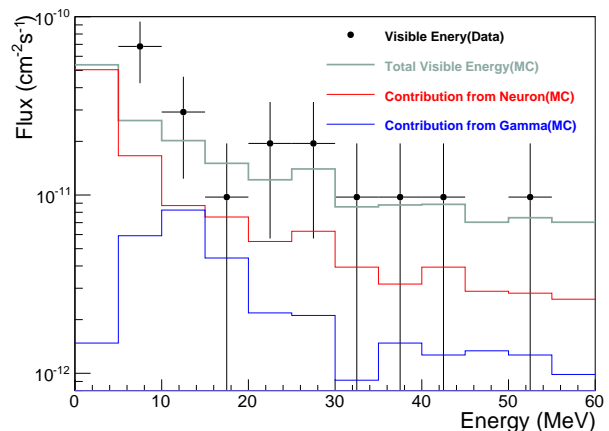


FIG. 16: The nuclear recoil events obtained from the NR band in FIG. 13. The solid dots are the visible energies “seen” by the PMTs. The solid blue and red lines stand for the nuclear recoils caused by gamma rays and neutrons, respectively. The gray line is the simulated total NR response to the showers. A factor of 1/1.21 is also applied to the simulated NR curves here in order to match the normalization assumed for the ER response.

detector. As shown in FIG. 15, gamma rays break ^{12}C nucleus through reaction of $^{12}\text{C}(\gamma, 3\alpha)$ when the energy of gamma ray exceeding 13 MeV. Those α recoils are classified as NR events and show up in the NR band. The NR events produced through muon-nucleus processes are found to be negligible in the data.

Extracting the NR band from FIG. 13 (right plot), the detector response to nuclear recoils is shown in FIG. 16 (solid dots). The simulated detector response to nuclear recoils takes the input muon showers from the results in FIG. 11. The normalization factor of 1.21 is also applied to all simulated NR responses (solid lines in FIG. 16). This reduces the cosmogenic neutron flux

from 5.72×10^{-9} /cm²/s down to 4.73×10^{-9} /cm²/s in FIG. 11. Subsequently, the cosmogenic gamma-ray flux is reduced from 8.57×10^{-7} cm⁻²s⁻¹ to be 7.08×10^{-7} cm⁻²s⁻¹. The simulated NR contributions from neutrons (red line) and gamma rays (blue line) are separated. It indicates that gamma rays induced nuclear recoils are comparable to that of neutrons in the energy range of about 15 MeV. In addition, the cosmogenic high-energy gamma rays are very penetrating and could undergo photo-nuclear reaction to create neutrons inside the shield that is close to the detector. Therefore, the cosmogenic high-energy gamma rays are an important source of background to rare event physics experiments.

V. DISCUSSION AND CONCLUSION

The muons at the Earth's surface are utilized to calibrate the detector response to high energies. The result is a reasonable approximation by assuming a linear relation between the light output and the energy deposition at high energies. Neutrons at the Earth's surface are measured using the large liquid scintillation detector. The discrepancy between the measured data and the simulated result above 20 MeV is within a factor of 2. A full calibration using high energy neutron beam would help in terms of the energy and position calibrations for high energies so that we can confidently identify the sources of issue, either from the detector response itself or from the external input.

An approach to calculate the quenching factor for nuclear recoils in scintillators is proposed. This approach can be extended to other type of scintillation detectors.

Muon and neutron fluxes at Soudan Mine are simulated by taking into account the surface mountain profile and rock density. Since the reality of the rock configuration is more complicated, the simulated results have to be justified by the measurement in terms of their absolute fluxes. The lower end of measured visible energy from neutron band is limited by the random noise (~ 4 MeV). Given the quenching effect and the energy transfer from neutron-ion collisions, the measured neutrons should have kinetic energies above ~ 10 MeV according to this 4 MeV threshold. The highest visible energy of ~ 50 MeV in the neutron band accounts for the potential incident neutrons with energy about a few hundred MeV

depending on the incident angle. This is the first time we have directly seen such high energy cosmogenic neutron events in an underground detector.

The statistical error of the muon measurement is about 1.23% while it is 22.94% one the average for the neutron flux due to the relatively lower intensity at the mine. The dominant systematic uncertainty for muons comes from a 5% variation in total muon rates observed in the experiment. In addition, the energy and position calibration contributed to about 3% uncertainty determined using the Monte Carlo simulation. For neutrons, in addition to the inherited systematics from the parent muons, the systematic uncertainty is mainly from the complicated quenching factor matrix at level of about 6% to the total flux determined by the Monte Carlo simulation. Adding the sources of systematic uncertainties in quadrature, the final muon flux is determined to be $(1.65 \pm 0.02(sta.) \pm 0.1(sys.)) \times 10^{-7}$ cm⁻²s⁻¹ and the measured neutron flux ($E_n > 10$ MeV) is $(4.73 \pm 1.1(sta.) \pm 0.4(sys.)) \times 10^{-9}$ cm⁻²s⁻¹. The former is in a good agreement with the previous measurement made by the MINOS far detector [49]. The latter agrees with the prediction made by Ref. [16] very well.

In summary, we have demonstrated the capability to detect cosmogenic neutrons underground with a large liquid scintillation detector. Although there are only a dozen of events detected in the NR band in two years, they are well separated from electron recoils. Due to relatively low cost of the whole detector, an array of hundreds of such detectors would be able to collect the sufficient statistics for studying cosmogenic neutrons in the underground laboratory.

VI. ACKNOWLEDGEMENT

The authors wish to thank Fred Gray, Keenan Thomas, Anthony Villano and Priscilla Cushman for their invaluable suggestions and help. We would also like to thank Christina Keller, Angela Chiller, and Wenzhao Wei for careful reading of this manuscript. This work was supported in part by NSF PHY-0758120, PHYS-0919278, PHYS-0758120, PHYS-1242640, DOE grant DE-FG02-10ER46709, the Office of Research at the University of South Dakota and a 2010 research center support by the State of South Dakota.

-
- [1] V. Trimble, Annual Review of Astronomy and Astrophysics, 25 (1987) 425-472.
 - [2] R. Bernabei et al. (DAMA Collaboration), Riv. N. Cim. 26 (2003) 1-73.
 - [3] Z. Ahmed et al. (CDMS II Collaboration), Science, 327 (2010) 1619-1621.
 - [4] C. E. Aalseth et al. (CoGeNT Collaboration), Phys. Rev. Lett., 107 (2011) 141301.
 - [5] G. Angloher et al. (CRESST-II Collaboration), Eur. Phys. J. C, 72 (2012) 1971.
 - [6] M. Barnabe-Heider et al. (PICASSO), Phys. Lett. B 624 (2005) 186.
 - [7] G. J. Alner et al. (UKDMC), Phys. Lett. B 616 (2005) 17.
 - [8] V. A. Kudryavtsev (UKDMC), in the Fifth International Workshop on the Identification of Dark Matter, Edinburgh, Scotland, 2004.
 - [9] A. Benoit et al. (EDELWEISS Collaboration), Phys.

- Lett. B 616 (2005) 25.
- [10] T. A. Girard et al., Phys. Lett. B 621 (2005) 233.
- [11] S. Desai et al. (Super-Kamiokande Collaboration), Phys. Rev. D 70 (2004) 083523.
- [12] Z. Ahmed et al. (CDMS and EDELWEISS Collaborations), Phys. Rev. D 84 (2011) 011102.
- [13] E. Aprile et al. (XENON Collaboration), Phys. Rev. Lett. 109 (2012) 181301.
- [14] D. S. Akerib et al. (LUX collaboration), Phys. Rev. Lett. 112, 091303 (2014), arXiv:1310.8214
- [15] R. Agnese et al. (SuperCDMS Collaboration), arXiv:1402.7137.
- [16] D.-M. Mei and A. Hime, Phys. Rev. D 73 (2006) 053004.
- [17] Y.-F. Wang, et al., Physical Review D 64 (2001) 013012.
- [18] V. Kudryavtsev, N. Spooner, J. McMillan, Nuclear Instruments and Methods in Physics Research A 505 (2003) 688698.
- [19] H. Araujo, V. Kudryavtsev, N. Spooner, T. Sumner, Nuclear Instruments and Methods in Physics Research A 545 (2005) 398411.
- [20] V. Kudryavtsev, L. Pandola, V. Tomasello, The European Physical Journal A 36 (2008) 171180.
- [21] G. Gorshkov, V. Zyabkin, R. Yakovlev, Soviet Journal of Nuclear Physics- USSR 18 (1974) 5761.
- [22] M. Marino, et al., Nuclear Instruments and Methods in Physics Research A 582 (2007) 611620.
- [23] H. Araujo, et al., Astroparticle Physics 29 (2008) 471481.
- [24] S. Abe, et al., Physical Review C 81 (2010) 025807.
- [25] G. Bellini et al., JINST, 6, p05005, 2011.
- [26] L. Reichhart et al. Astropart. Physics 47 (2013) 67-76.
- [27] R. A. Cecil B. D. Anderson and R. Madey, Nucl. Instr. and Meth. 161 (1979) 439.
- [28] R. Batchelor, W. B. Gilboy, J. B. Parker and J. H. Towle, Nucl. Instr. and Meth. 13 (1961) 70.
- [29] V. V. Verbinski, W. R. Burrus, T. A. Love, W. Zobel and N. W. Hill, Nucl. Instr. and Meth. 65 (1968) 8.
- [30] K. Gul, A. A. Naqvi and H. A. Al Juwair, Nucl. Instr. and Meth. A 278 (1989) 470.
- [31] A. Aksoy et al., Nucl. Instr. and Meth. A 337 (1994) 486-491.
- [32] N. Nakao et al., Nucl. Instr. and Meth. A 362 (1995) 454-465.
- [33] R. E. Textor and V. V. Verbinski, ORNL-4160, Oak Ridge National Laboratory (1968).
- [34] J. K. Dickens, ORNL-6463, Oak Ridge National Laboratory (1988).
- [35] C. Zhang, et. al., Nucl. Instr. and Meth. A 729 (2013) 138-146.
- [36] S. Agostinelli, et al, Nucl. Instr. and Meth. A 506 (2003) 250-303; K. Amako et al., IEEE Transactions on Nuclear Science 53 (2006) 270-278.
- [37] M. Guan, et. al., <http://escholarship.org/uc/item/6jm8g76d>
- [38] <http://www.city-data.com/city/Vermillion-South-Dakota.html>
- [39] M. S. Gordon, et. al., IEEE Transactions on Nuclear Science 51 (2004) 3427-3434.
- [40] J. B. Birks and F. A. Black, Proc. Phys. Soc. A 64 (1951) 511i.
- [41] G. Bruno, JINST 8 (2013) T05004.
- [42] H. Wan Chan Tseung, J. Kaspar, N. Tolich, Nucl. Instr. and Meth. A 654 (2011) 318-323.
- [43] <http://physics.nist.gov/PhysRefData/Star/Text/ESTAR.html>
- [44] <http://physics.nist.gov/PhysRefData/Star/Text/PSTAR.html>
- [45] <http://physics.nist.gov/PhysRefData/Star/Text/ASTAR.html>
- [46] P. Adamson et al. (MINOS Collaboration), Phys. Rev. D 73 (2006) 072002.
- [47] D. S. Akerib et al. (CDMS Collaboration), Phys. Rev. Lett. 93 (2004) 211301.
- [48] C. E. Aalseth et al. (CoGeNT Collaboration), Phys. Rev. Lett. 106 (2011) 131301.
- [49] P. Adamson et al. (MINOS Collaboration), Phys. Rev. D 81 (2010) 012001.
- [50] <http://srtm.csi.cgiar.org/>
- [51] <http://homepages.spa.umn.edu/~schubert/far/s2rock/position.html>
- [52] K. Ruddick, Underground Particle Fluxes in the Soudan Mine, Internal Note NuMI-L-210, 1996.
- [53] M. S. Gordon, et. al., IEEE Transactions on Nuclear Science 51 (2004) 3427-3434.
- [54] N. Pastika, Bachelors Thesis, University of Minnesota, 2008.
- [55] V. A. Kudryavtsev, Computer Physics Communications, 180 (2009) 339-346.
- [56] M. Moszyński, et al., Nucl. Instr. and Meth. A 343 (1994) 536-572.
- [57] M.B. Chadwick et al., Nucl. Data Sheets 112(2011)2887.